TAO, Vol.7, No.2, 209-224, June 1996

Further Studies of a Prefrontal Convective Rainband During TAMEX IOP 13 Part II: Kinematic Structure and History

ROBERT PASKEN[1] and YEONG-JER LIN[2]

(Manuscript received 12 June 1995, in final form 26 January 1996)

ABSTRACT

Doppler radar data collected at 7-min intervals by the TOGA radar during TAMEX IOP 13 were used to investigate the time-dependent kinematic structure of the Mei-Yu front and the associated rainband as it made landfall on the western shore of Taiwan. Using RHI cross sections, chosen to be nearly perpendicular to the approaching Mei-Yu front, the vertical velocities and divergences were calculated. Using these data, the time-dependent kinematic structure of the Mei-Yu front and prefrontal convective rainband were analyzed. A careful analysis shows that high speed mid-level dry flow pushes the high reflectivity cores at the Mei-Yu front southeastward into the warm sector. In addition, evaporative cooling associated with a strong dry-air intrusion at mid to upper levels combines with precipitation loading to create convective downdrafts in a wide-spread area ahead of the Mei-Yu front. The low-level cold outflow from the downdraft interacts with the moisture-rich southwest monsoon flow creating a gust front. A smaller portion of the downdraft is also directed back to the Mei-Yu front sustaining the front. These structures provide further evidence supporting the conceptual model put forth in Lin *et al.* (1992).

(Key words: TAMEX, Long-lived rainband, Radar meteorology, Mesometeorology)

1. INTRODUCTION

In Part 1 of this paper (Lin *et al.* 1996), we presented additional observational evidence to support the conceptual model of the prefrontal rainband associated with the Mei-Yu front during TAMEX IOP 13 (Taiwan Area Mesoscale Experiment Intensive Observing Period 13) described in Lin *et al.* (1992). Lin *et al.* (1992) proposed that the Mei-Yu front played an important role in the initiation and maintenance of the rainband at the start of the rainband's

[1] Dept. of Science and Mathematics, Parks College of Saint Louis University, Cahokia, IL 62206, U.S.A.

[2] Dept. of Earth and Atmospheric Sciences, St. Louis University, St. Louis, MO 63103, U.S.A.

life. However, the Mei-Yu front lost its direct influence on the rainband near the coastline as the system moved down the central west coast of Taiwan. As the rainband moved away from the front, gust fronts were formed by the cells at the leading edge of the system. These gust fronts interacted with the southwest monsoon flow creating new convective cells at the gust fronts. At the same time, the southwest portion of the Mei-Yu front (about 50 to 60 km west of the Taiwan coast) continued to lift the moisture-rich air in the southwest monsoon flow to create new convective cells. These convective cells traveled east following the westerly flow at low levels. These cells merged with the older cells in the rainband near the west coast, thereby prolonging the life of the rainband.

To support this conceptual model, conventional radar data were used to show how the rainband moved away from the Mei-Yu front along the western coast. Careful examination of 11 hours of Kaohsiung conventional radar data shows the rainband moving away from the Mei-Yu front along the western coast (see Figure 1 in Part 1). Surface data from stations along the western coast further support the rapid movement of the rainband away from the Mei-Yu front. Using 46 minutes of TOGA reflectivity data, an example of the cell merger was also shown (see Figure 4 in Part 1). A convective cell on the southwestern edge of the Mei-Yu front moved away from the Mei-Yu front, quickly moved eastward and merged with the rainband. Similar examples of the merger of convective cells at earlier times of IOP 13 were given in Li *et al.* (1995). The radial velocity and estimated convergence/divergence fields at the lowest level (0.25 km), from the TOGA radar, as presented in Figures 7 and 8 of Part 1, clearly showed the location of the gust front as a region of weak speed convergence further supporting the conceptual model.

The other features proposed in the conceptual model require a more detailed wind field than provided by the conventional radar data or the simple radial velocity data presented in Part 1. Although dual-Doppler data were available from the TOGA and CP-4 radars, a careful analysis of these data is extremely time-consuming and has not yet been completed. Furthermore, the main features of the rainband moved to an area close to the baseline between the two radars after 0700 LST (local standard time) 25 June, thereby creating additional difficulties for a dual-Doppler analysis.

To test the other features of the conceptual model, an experiment was conducted to determine if qualitative and quantitative information could be obtained from a single-Doppler analysis rather than a dual-Doppler analysis. Since dual-Doppler analyses at 0653 and 0700 LST were already reported in Lin *et al.* (1992) and Lin *et al.* (1993), the results of the single-Doppler analysis could be compared directly with cross sections from the dual-Doppler analysis. These experiments have shown that a single-Doppler analysis is capable of recovering the major features present in the dual-Doppler analysis. Using this single-Doppler analysis technique, the kinematic structure and evolution of the Mei-Yu front and the associated prefrontal rainband can be described.

Single Doppler radars have been used by many other researchers to examine the vertical structure of convective storms in other geographical regions. Browning and Harold (1970) used a single-Doppler radar to examine the structure of a narrow cold frontal band. Wakimoto (1982) used a single-Doppler radar during NIMROD (Northern Illinois Meteorological Research On Downburst) to explore the structure of a thunderstorm gust front in the lowest few kilometers above the ground.

A single-Doppler analysis of the Mei-Yu front and leading edge of the rainband (gust front) was considered possible because of the organized structure of the Mei-Yu front and the associated prefrontal rainband (Lin *et al.* 1992). The dual-Doppler analysis for 0653

and 0700 LST revealed that the magnitude of the horizontal divergence along the beam is much larger than that tangent to the beam. This finding strongly suggests that the simplified anelastic continuity equation may be employed to estimate the vertical velocity in a direction normal to the frontal system using a single-Doppler radar.

The goal of this study is to provide additional support for the conceptual model of a prefrontal rainband in IOP 13 put forth by Lin *et al.* (1992), in the form of the time-dependent kinematic structure of the Mei-Yu front and the associated prefrontal rainband. Using a single-Doppler analysis technique, a kinematic analysis of the structure of the Mei-Yu front and prefrontal rainband was performed at 7-min intervals from 0653 to 0810 LST. The kinematic structure determined from this analysis shows that high-speed mid-level flow pushes the precipitation products ahead of the Mei-Yu front. In addition, the combined effects of evaporative cooling, associated with a strong dry air intrusion at mid to upper levels, and precipitation loading in the high reflectivity core region create convective downdrafts ahead of the Mei-Yu front. The major portion of the low-level cold outflow from the downdraft interacts with the moisture-rich southwest monsoon flow in a broad area southeast of the front creating a gust front. A smaller portion of the descending downdraft air is also directed back to the Mei-Yu front thereby sustaining the low-level convergence at the leading edge of the front. These features are the essential components of the Lin *et al.* (1992) model.

2. METHODOLGY

Recovering the three-dimensional wind field of a storm normally takes at least two Doppler radars. The terminal velocity is estimated from the radar reflectivity, and the vertical velocity is computed by integrating the anelastic continuity equation downwards from the top of the storm with a variational adjustment similar to Ray *et al.* (1980) and Lin *et al.* (1986). Under special circumstances, it is possible to recover the wind field using only one Doppler radar. As mentioned earlier, Browning and Harrold (1970) used a single-Doppler radar to recover the winds in a mid-latitude cold front, and Wakimoto (1982) used a single-Doppler radar to recover the winds in a downburst during the NIMROD experiment. In each of these cases, the cross-beam component of the wind shear was assumed to be zero or small enough to be ignored when compared to the along-beam component in the anelastic continuity equation. Eliminating the cross-beam term reduces the number of unknowns to three; namely, 1) the radial velocity, 2) the vertical velocity and 3) the terminal velocity. As with the dual-Doppler case, the terminal velocity, V_t, can be recovered from the radar reflectivity via a $Z - V_t$ relationship and the vertical velocity can be calculated from the anelastic continuity equation.

As shown in Part 1 of this paper, the Mei-Yu front and prefrontal rainband consisted of many convective cells embedded within a widespread area ahead of the front. Although convective cells were distributed along the length of the Mei-Yu front, the most significant changes in the structure of both the Mei-Yu and gust fronts occurred in a direction normal to the front. Ahead of the front, the low-level jet (LLJ) was the dominant feature with nearly uniform flow parallel to the front. Behind the front, the flow was nearly normal to the front. Along this normal direction, we assume the derivatives of the cross-beam component are much smaller than the derivatives parallel to the beam in the anelastic continuity equation. This assumption is justified by the results obtained from our dual-Doppler analysis at 0653 and 0700 LST 25 June (see Lin *et al.* 1992).

The anelastic continuity equation in a cylindrical coordinate system (r, θ, z, t) with the origin at the radar site can be written as:

$$\frac{\partial(\rho_0 r V_r)}{r\partial r} + \frac{\partial(\rho_0 V_\theta)}{r\partial\theta} + \frac{\partial(\rho_0 w)}{\partial z} = 0 \,, \tag{1}$$

where V_r is the radial velocity component, V_θ is the tangential velocity component, w is the vertical velocity component, r is the radial distance to the radar, θ is the azimuth angle, and the other symbols have their usual meanings. As discussed earlier, if we assume that the cross-beam components ($\partial/\partial\theta$ terms) are small compared to the components parallel to the beam ($\partial/\partial r$ terms), then the simplified form of the anelastic continuity equation can be written as:

$$\rho_0(z)\left[\frac{V_r}{r} + \frac{\partial V_r}{\partial r}\right] + \frac{\partial(\rho_0 w)}{\partial z} = 0 \,, \tag{2}$$

where $\frac{V_r}{r} + \frac{\partial V_r}{\partial r} = D$ is the horizontal divergence in the plane of the vertical cross section, and $\rho_0(z)$ is the observed environmental air density. The radial velocities recovered by the radar are the vector sum of the horizontal velocities, V_r, the terminal velocities, V_t, and the vertical velocities w of the targets (see Figure 1). If the elevation angle ϕ is small enough and the vector sum $V_t + w$ is small compared to V, then V_r can be found from:

$$V_r = V cos\phi \,, \tag{3}$$

where V is the measured radial velocity (see Figure 1). Since the elevation angle ϕ is small ($< 20°$) in this study, the horizontal velocities can be recovered from (3) above with reasonable accuracy. In this simplified form, the anelastic continuity equation can be integrated downwards starting at the top of the storm to give the vertical velocity at each successive layer downward. The vertical velocity at z_1 can be found from the expression:

$$w_1 = \left(\frac{\rho_{02}}{\rho_{01}}\right) w_2 + \frac{\overline{\rho_0(z)D}}{\rho_{01}}\delta z \,, \tag{4}$$

where the overbar means an average over the layer, D is the horizontal divergence as defined earlier, and $\delta z = z_2 - z_1$ with $z_2 > z_1$.

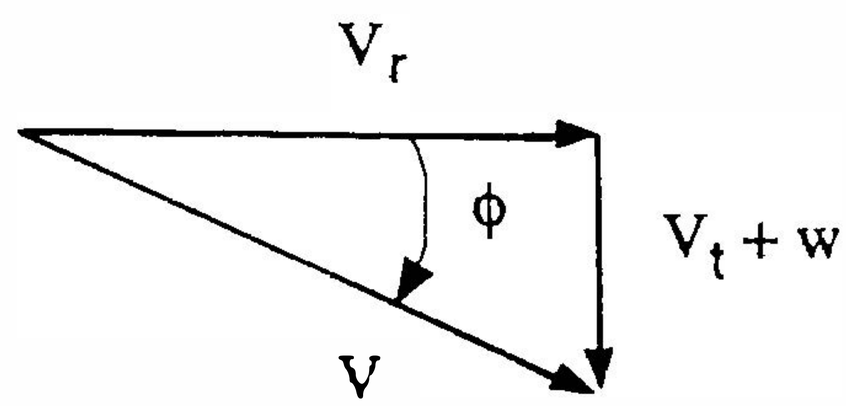

Fig. 1. Relationship between the radial velocity recovered by the radar and the radar winds used in the analysis.

The vertical velocity computed from (4) is subject to errors as a result of the accumulation of errors in the divergence field. Experiments conducted for both the single- and dual-Doppler cases show that the errors in the computed vertical velocity field are minimized when a downward integration is performed (e.g., Ray *et al.* 1980). The magnitude of the errors in the vertical velocity field is a function of the quality of the wind field derived from the radial velocities. To minimize these errors, a variational adjustment is made to the "observed" values of w to find the "true" values of w. These adjustments are made using the methods suggested by Ziegler *et al.* (1983) and Lin *et al.* (1986).

To test the single-Doppler analysis technique, TOGA and CP-4 data for 0653 and 0700 LST 25 June were used to conduct both a single-Doppler and a dual-Doppler analysis. The TOGA radar was chosen for both the dual-Doppler cross section and the single-Doppler analysis because it was well situated relative to the Mei-Yu front at the times of analysis. Figure 2 is reproduced from Lin *et al.* (1993), see their Figure 2a, displaying the system-relative winds with the reflectivity contours superimposed for 0.75 km at 0701 LST 25 June. Line AB in Figure 2 shows the cross section considered in the experiments. This cross section passes through TOGA and a convective cell in the rainband and is perpendicular to the Mei-Yu front. Fields of the system-relative wind, vertical velocity, reflectivity and streamline analysis for 0701 LST obtained from the dual-Doppler analysis along line AB are shown in Figure 3 and those derived from the single-Doppler radar along the same line are shown in Figure 4.

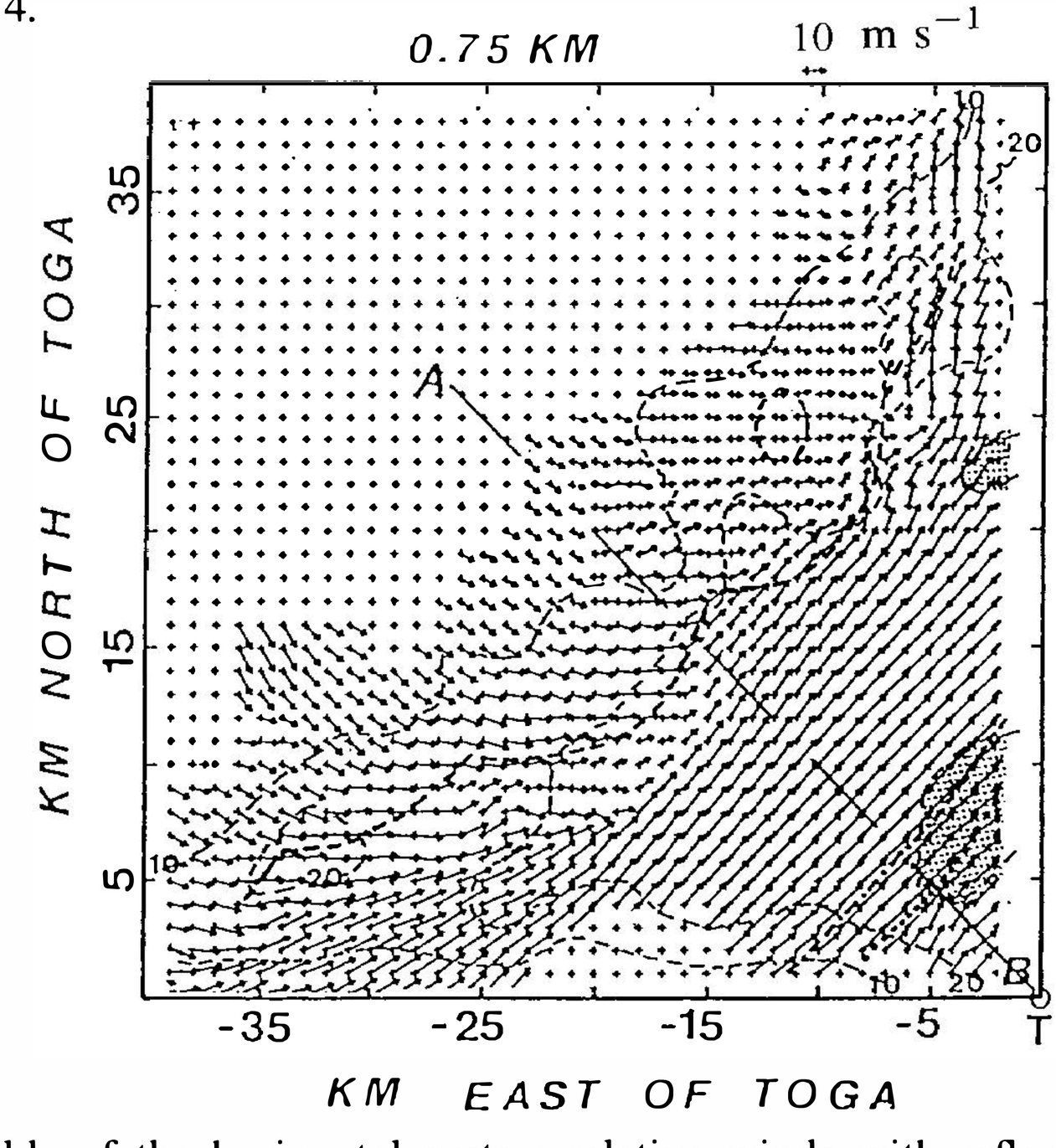

Fig. 2. Fields of the horizontal system-relative winds with reflectivity contours superimposed for 0.75 km at 0701 LST 25 June 1987. Reflectivities greater than 30 dBZ are shaded. The heavy dashed line shows the wind-shift line corresponding to the position of the Mei-Yu front. The location of the TOGA (T) radar and the location of the cross-sections (line AB) are indicated. Distances are in kilometers east and north of TOGA (T). Adapted from Lin *et al.* (1993).

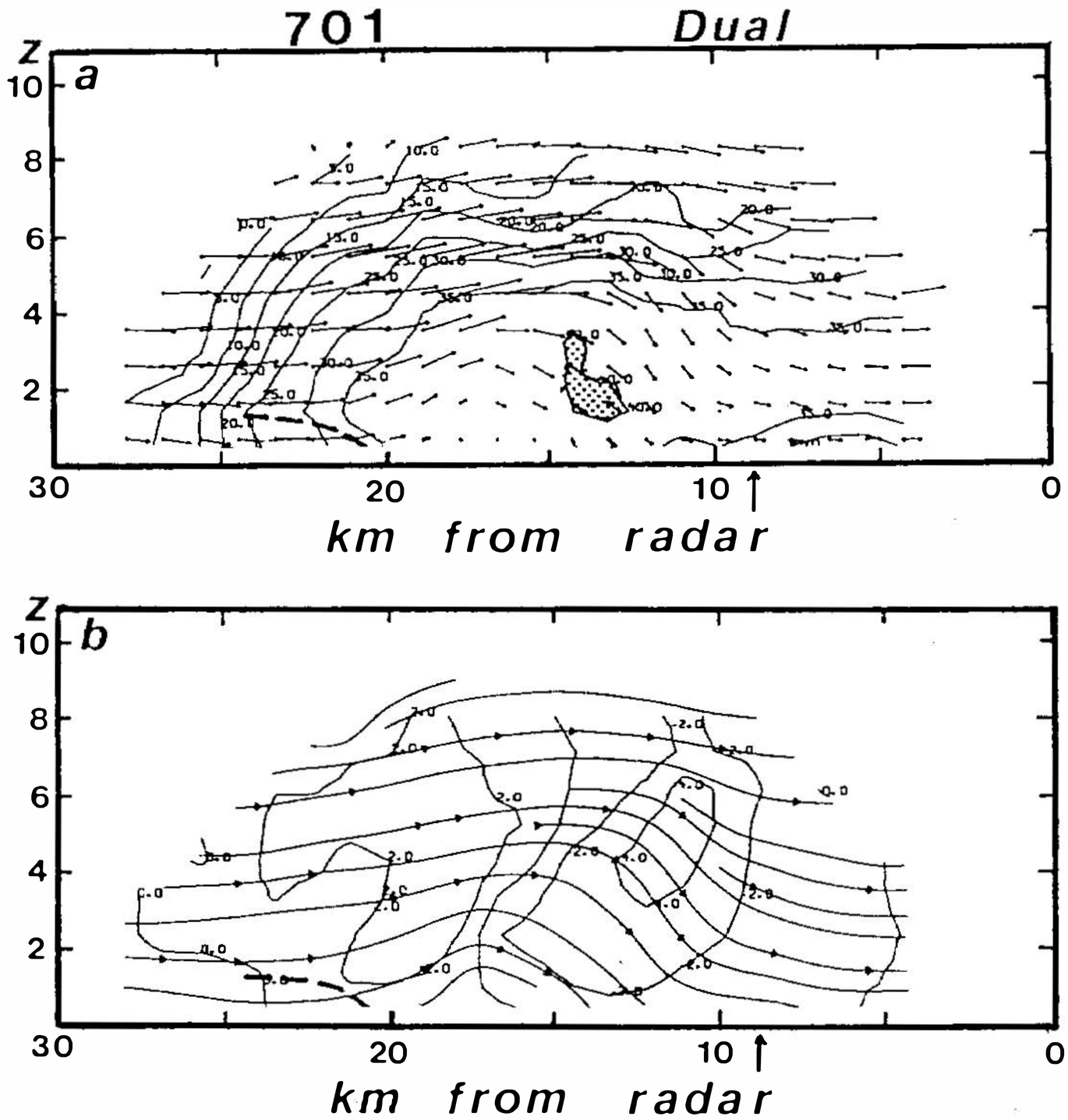

Fig. 3. The vertical cross section along line AB in Figure 2 showing (a) the system-relative winds with reflectivity contours superimposed and (b) vertical velocity contours with streamlines superimposed at 0701 LST 25 June based on a dual-Doppler analysis. The heavy dashed line and arrow mark the position of the Mei-Yu and gust fronts, respectively. The contour interval for reflectivity is 5 dBZ and 2 m s^{-1} for vertical velocity. Distances are in kilometers from TOGA.

As depicted in Lin *et al.* (1992), (section 5c and Figures 21 and 22), the reflectivity, airflow and vertical velocity fields along the cross-sections, in a direction perpendicular to the front, show that a convective updraft formed at the leading edge of the front. In the high reflectivity region on the warm side of the front (right side of the figure), a convective downdraft prevailed. This downdraft resulted in a low-level diverging flow. Part of this diverging flow moved toward the southeast and met with the moisture-rich monsoon air in the warm sector, producing a secondary updraft ahead of the GF (see Figure 22 in Lin *et al.*). In the middle and upper layers, the strong northwesterly flow ($\approx$ 20 m s^{-1}) dominated. This strong northwesterly flow aloft elongated the reflectivity core to the southeast in a manner similar to that described in Lin *et al.* (1992).

Inspection of the **dual-Doppler** analysis (Figure 3) reveals many of the features described in the Lin *et al.* (1992) paper. The reflectivity field (Figure 3a) shows a broad region of reflectivities 30 dBZ or greater ahead of the front (heavy dashed line) and extending nearly to the radar. Conversely, reflectivities were weak in the shallow region behind the front corresponding to the stratiform region. Note that the strongest reflectivities were confined to a

region below 6 km and are vertically oriented. A region of much lower reflectivities, overlays this region of higher reflectivities. The vertical velocity field (Figure 3b) corresponds well with the reflectivity field in Figure 3a. About 20 km from the radar, there is a moderate updraft induced by the Mei-Yu front advancing into the warm moist air of the prevailing southwesterly flow (see Figure 2). This moderate updraft is embedded in a larger region of positive vertical velocities. The 4–6 m s^{-1} downdraft 11 km from the radar appears to be induced by a combination of the evaporative cooling induced by the drier air above 6 km (the lower reflectivities mentioned earlier) and precipitation loading in the high-reflectivity core at mid-levels. The diverging flow at the surface created by this downdraft is clearly seen in the streamline analysis shown in Figure 3. This diverging flow creates the gust front (GF) near the surface. The streamline analysis (Figure 3b) clearly defines the location of the Mei-Yu and gust fronts and it strengthens the relationship between the downdraft, the reflectivity maximum and the gust front. This analysis shows that the gust front occurs at the surface where the mid-level flow is diverted toward the surface by the downdraft (created by the evaporative cooling and precipitation loading discussed earlier). The Mei-Yu front is also clearly delineated in the streamline analysis. The strong rear-to-front northwesterly flow behind the front collides with the southwesterly monsoon flow to create the Mei-Yu front. At the Mei-Yu front the streamlines rise sharply marking the convective zone. The convection is then blown downstream by the strong mid-level winds.

Figure 4a presents the **single-Doppler** reflectivity field taken along the same line as the dual-Doppler analysis. The single-Doppler analysis winds extend all the way to the radar. The dual-Doppler analysis does not, because the dual-Doppler analysis requires that both radars have reflectivities above a minimum level and the CP-4 radar has consistently lower reflectivities due to attenuation. Because CP-4 was looking down the length of the Mei-Yu front, attenuation reduced the signal strength to the point where a dual-Doppler analysis could not be done. Since the TOGA radar was closer to the front, the attenuation is less and the single-Doppler analysis is able to recover the velocities. The single-Doppler analysis shows the reflectivity maxima and minima located in the same regions and are nearly the same magnitude. Since the single-Doppler analysis is describing the same physical mechanisms as the dual-Doppler analysis, the results are comparable. The vertical velocities derived from the single-Doppler analysis (Figure 4b) recovers the same features as those in the dual-Doppler analysis. The Mei-Yu front is marked by the 4 m s^{-1} updraft located about 21 km from the TOGA radar where the Mei-Yu front lifts the warm moist southwesterly flow. The location and magnitude of this updraft is comparable to that derived from the dual-Doppler analysis (Figure 3b); however, it is more vertically oriented and stronger in the single-Doppler analysis. The downdraft associated with the gust front ahead of the Mei-Yu front is stronger and less elongated to the southeast. None the less, the downdraft has a comparable magnitude and location. The streamline analysis using the single-Doppler winds is similar to the dual-Doppler streamline analysis (Figure 3b). The single-Doppler streamlines show the location of the Mei-Yu front more clearly along with an anti-cyclonic gyre just ahead of the front.

It must be pointed out that the approximate positions of the Mei-Yu front (heavy dashed line) and the GF (vertical arrow) shown in Figure 4 and the remaining analysis times (Figures 7–>10) are based on the single-Doppler analysis reported in Part I of this study (see Figures 7 and 8 in Part I). We employed the radial velocity and unadjusted divergence fields in the lowest layer (0.25 km) to determine the positions. However, the weak convergence at the GF seen in the unadjusted convergence/divergence field is no longer seen in Figure 4 due to the application of variational adjustments to the divergence field in order to calculate the vertical velocity field. This point must be kept in mind whenever the location of the GF is examined in Part II.

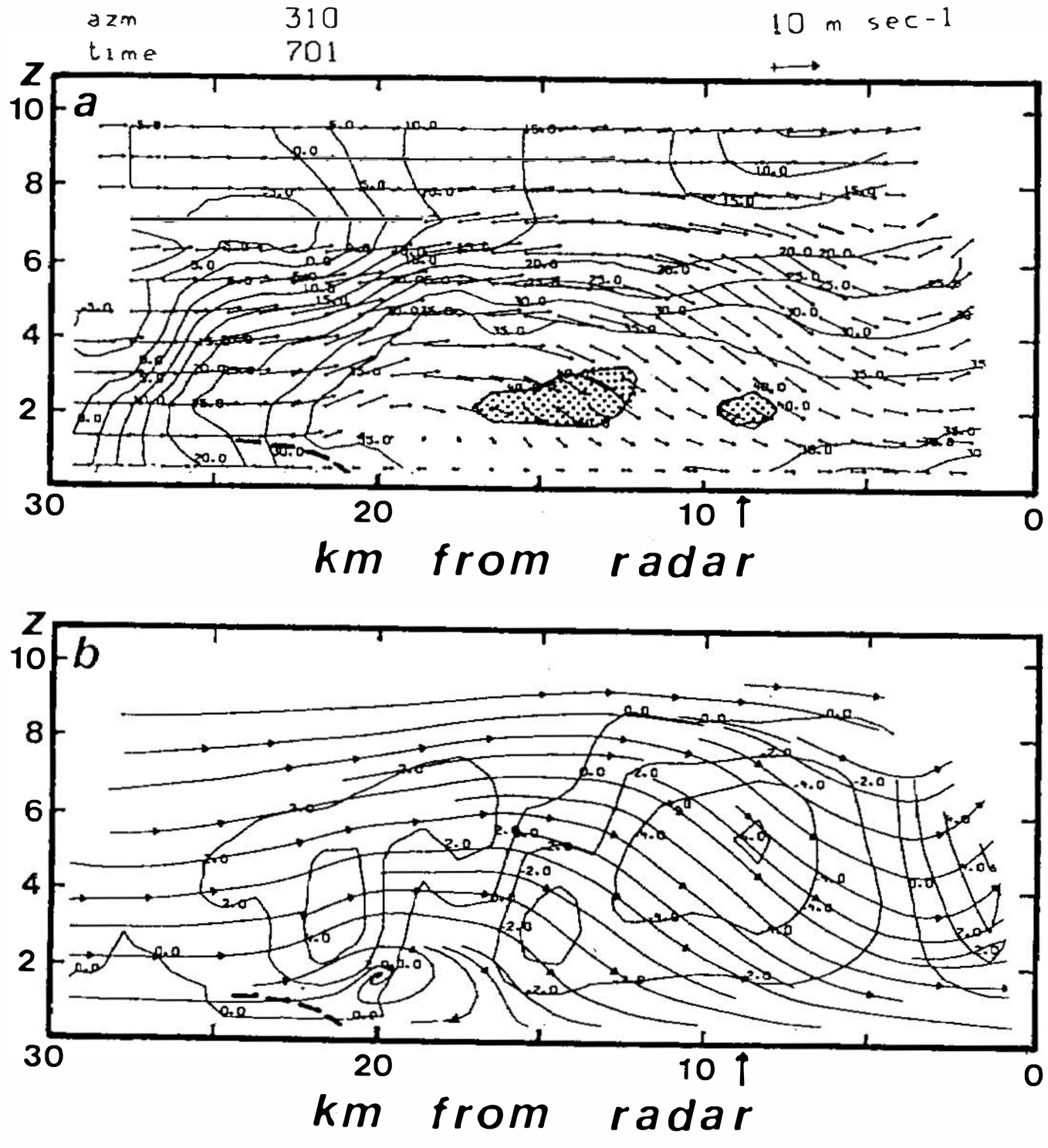

Fig. 4. The vertical cross section along the 310° radial using data from TOGA showing (a) the system-relative winds with reflectivity contours superimposed and (b) vertical velocity contours with streamlines superimposed at 0701 LST 25 June based on a single-Doppler analysis. The heavy dashed line and arrow mark the position of the Mei-Yu and gust fronts, respectively. The contour interval for reflectivity is 5 dBZ and 2 m s^{-1} for vertical velocity. Distances are in kilometers northwest of TOGA.

Figures 5 and 6 are the dual- and single-Doppler analysis for 0653 LST along the same radial as in Figures 3 and 4. Examination of these figures shows that the single-Doppler analysis is able to recover the features of the dual-Doppler analysis. Although the dual-Doppler analysis has the reflectivity maximum more vertically oriented than the single-Doppler analysis, the features are correctly placed and of the same magnitude. The vertical velocity fields are also more vertically oriented, but as with the reflectivity field, they are in the same locations and nearly the same magnitudes. The most significant difference between the dual- and single-Doppler analysis is a band of nearly zero vertical velocities extending from the top of the storm to about 5 km in the single-Doppler analysis. The dual-Doppler vertical velocity field extends the 2 m s^{-1} contours to the top of the storm. The downdraft ahead of the Mei-Yu front is more extensive in the single-Doppler case. As with the updraft over the Mei-Yu front, the downdraft extends almost to the top of the storm in the dual-Doppler case. The streamlines in both figures place the Mei-Yu and gust fronts in nearly the same location.

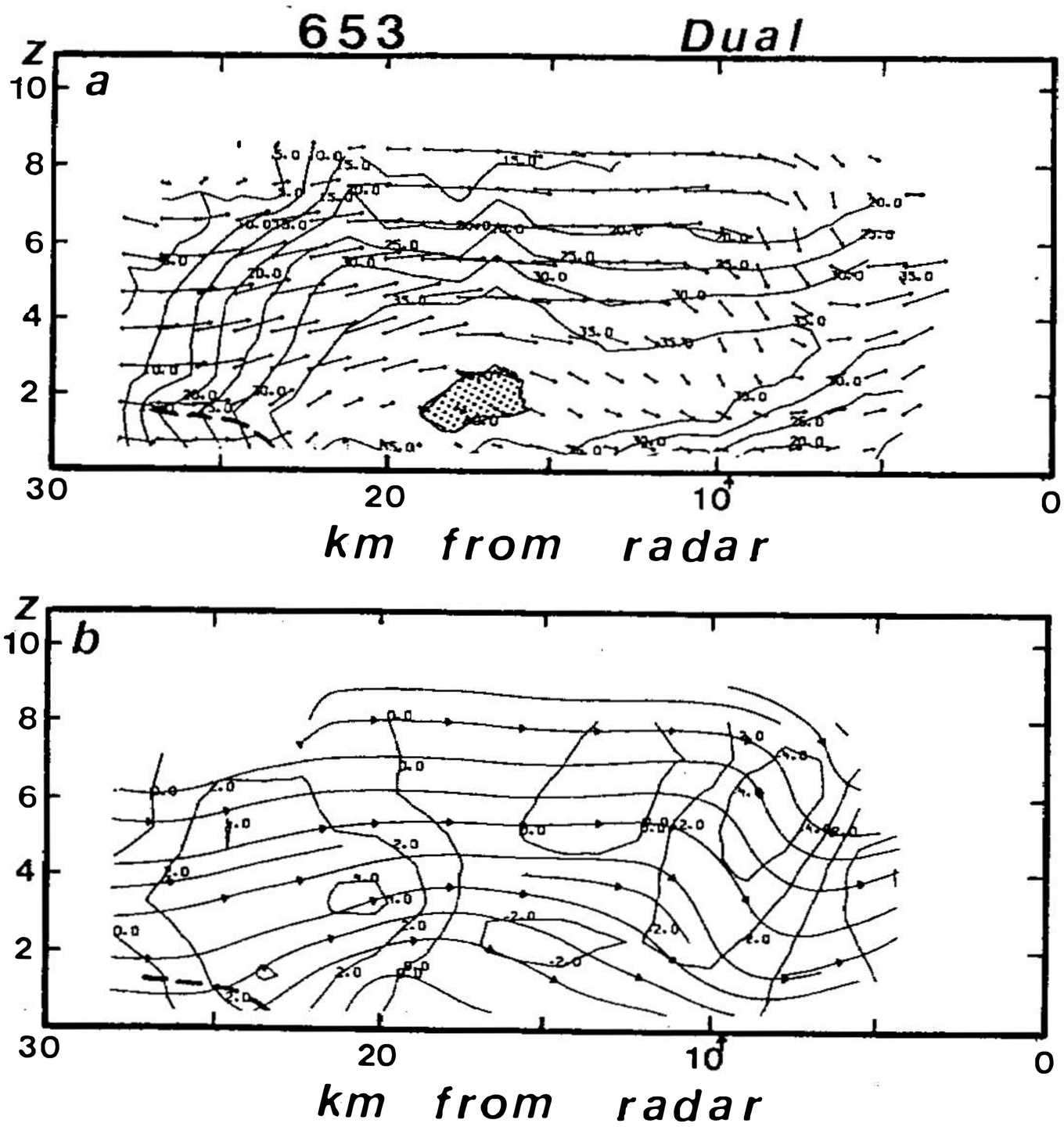

Fig. 5. As in Figure 3 except for the dual-Doppler analysis at 0653 LST 25 June.

In the comparison of the results of the dual- and single-Doppler analysis presented above, a single-Doppler analysis is capable of capturing the primary features of the Mei-Yu front and the gust front. The location and magnitude of the updraft and downdraft associated with the Mei-Yu and gust fronts are recovered by the single-Doppler analysis. The minor differences in the shape and magnitudes can be accounted for by the differences in analysis techniques and the additional information present in the dual-Doppler analysis. The strengths and magnitude of the important features are consistently recovered in both analysis times presented. From the results presented in the comparisons above, the single-Doppler analysis is capable of recovering the qualitative information about the structure of the Mei-Yu and gust fronts as they approach the TOGA radar.

3. DISCUSSION OF RESULTS

The RHI (range-height indicator) slices of the rainband were not part of the scanning strategy. The RHI used in this study were derived from the entire volume of vertically stacked PPI (plan-position indicator) scans. The azimuth angles selected for this study were nearly normal to the advancing rainband. Reflectivities and radial velocities were taken from the RHI slices, while horizontal velocities were determined from the geometry as discussed earlier. Vertical velocities were calculated from the simplified anelastic continuity equation by integrating downward from the storm top to reduce the accumulated error.

Reflectivities, vertical velocities and streamlines for the six time periods from 0653 to 0732 LST at 310° are shown in Figures 6,4,7,8,9 and 10. Contours are every 5 dBZ for

reflectivity and every 2 m s^{-1} for the vertical velocities. The Mei-Yu front is represented by the heavy dashed line. The range is in kilometers along the radial and heights are kilometers above sea level (ASL).

Figure 6 is the reflectivities, vertical velocities and streamline analysis for 0653 LST. A large area of 35 dBZ or greater exists in the region ahead of the front and extends to the radar site. There are three areas with reflectivities greater than 40 dBZ at 18, 12 and 6 km from the radar. These areas of higher reflectivities are located below 6 km ASL. Note that these convective cells are elongated to the southeast (toward the radar). As discussed in the previous section, the strong middle and upper level flow has stretched the reflectivity maximum downwind. The convective cell nearest the radar site is in the early stages of development and is produced by the weak gust front colliding with the warm, moist air advected into the region (Lin *et al.* 1993). The rainband is shallow with the 20 dBZ contour confined below 8 km.

The large area of downward motion located ahead of the front coincides with the high reflectivity region. These moderate downdrafts (4-6 m s^{-1}) appear to be induced by the precipitation loading from the high reflectivity cores. Also evident is a 4 m s^{-1} updraft centered near 26 km from the radar. This vertical motion is due to the interaction between the advancing cold front and the prevailing southwest flow. There exists an area of -20 m s^{-1} winds in the upper levels due to the high-level northwesterly flow, which is nearly parallel to the radar beam giving a nearly true indication of velocities.

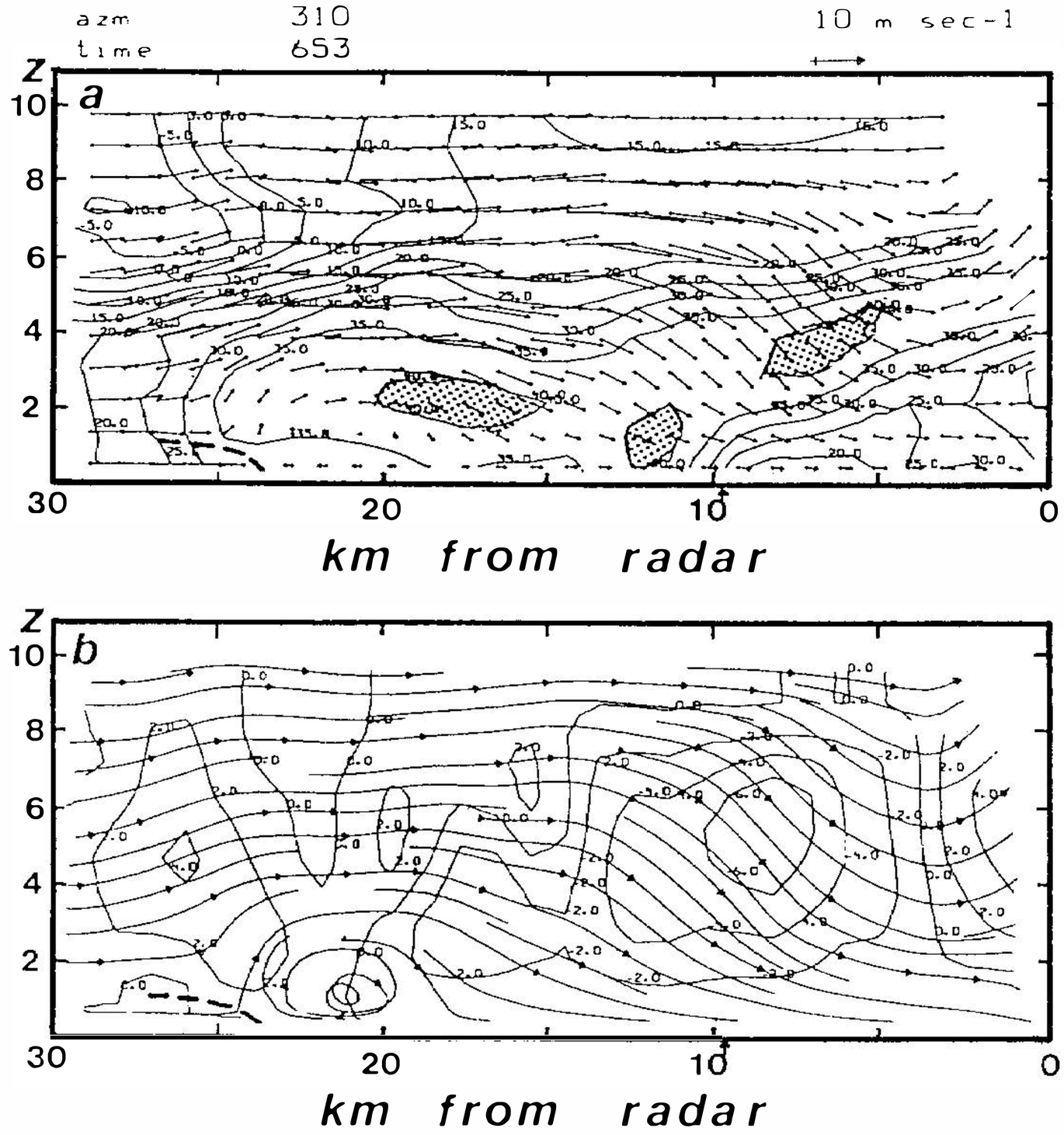

Fig. 6. As in Figure 4 except for the single-Doppler analysis at 0653 LST 25 June.

The streamline analysis clearly delineates the location of the Mei-Yu and gust fronts. The position of the Mei-Yu front is defined to be where the surface streamlines behind the Mei-Yu front are lifted over the flow ahead of the front. The southwesterly prefrontal flow at low levels, which is nearly perpendicular to the 310° azimuth radial, is delineated by the weak surface flow just ahead of the front. The streamlines also show the gust front to be located where the precipitation-induced downdraft has brought the mid-level flow to the surface. Careful analysis of the data file reveals weak convergence near r = 9 km where an area of high reflectivity has developed (see Lin *et al.* 1993). The gust front is characterized by weak convergence and slight wind shift (see Part 1 for details). This gust front shows the leading edge of the prefrontal rainband as it continuously moves slowly toward the TOGA radar. The streamline analysis also shows an anti-cyclonic gyre just ahead of the Mei-Yu front. This gyre is formed when the mid-level flow passes over the Mei-Yu front and then descends to the surface where it diverges. The majority of the diverging flow is directed to the southeast where it forms the gust front as described in Lin *et al.* (1993). A small portion of this diverging flow is directed back to the Mei-Yu front where it enhances the convergence there. The combination of the mid-level flow, the descending flow and the portion of the diverging flow directed back to the Mei-Yu front creates the anti-cyclonic gyre.

At 0701 LST (Figure 4), both the GF and the Mei-Yu front have advanced 1-2 km toward the radar. There is also a region of strong mid-level flow between 6-10 km ASL. The large region of 35 dBZ echoes shown in the last figure is still confined below 6 km and has lowered in the region closest to the radar. The small region of low reflectivities near 30 km at 0653 LST has pushed closer to radar extending this dry region to a point directly over the Mei-Yu front. The 40 dBZ echo 16 km from the radar at 0653 LST has risen and moved rapidly to near 9 km from the radar. Although the strength of the downdraft associated with the gust front has weakened, the size of the downdraft has increased substantially. The updraft located over the top of the Mei-Yu front has strengthened and lowered. The updraft has also become more vertically oriented. The streamline analysis shows a strengthening of the low-level anti-cyclonic gyre just ahead of the Mei-Yu front. As discussed above, part of the descending flow from the precipitation-induced downdraft is directed back toward the Mei-Yu front enhancing the convergence there. The streamline analysis clearly shows the air descending to the surface from mid-levels between the Mei-Yu and gust fronts. The majority of this flow is directed southeastward into the southwesterly monsoon flow as the gust front. The streamlines show that some of the descending flow, however, is directed back toward the Mei-Yu front where it enhances the convergence there in a manner similar to that described in Lin *et al.* (1993).

At 0708 LST (Figure 7), the Mei-Yu front has moved to 18 km from the radar, while the gust front has moved to about 8 km northwest of TOGA. Notice the vertical wind shear between 3 and 7 km ASL in the region ahead of the front. The veering winds are consistent with the vertical variation of the environmental winds described in Lin *et al.* (1992). In that study, the mean environmental winds at Makung over the strait revealed that veering occurred at most levels, showing the large-scale warm air advection favorable for MCS (mesoscale convective system) development (*e.g.*, Maddox 1980). The updraft over the Mei-Yu front continues to strengthen and lower, while the downdraft over the gust front regains its strength and shrinks in horizontal extent. A weak updraft develops at mid-levels ahead of the Mei-Yu front. This updraft appears to originate in the lobe of upward motion ahead of the Mei-Yu front seen on the last figure. As seen in the last two figures, the dry air intrusion (as marked by the low reflectivities) continues to push toward the radar from the northwest. Most of

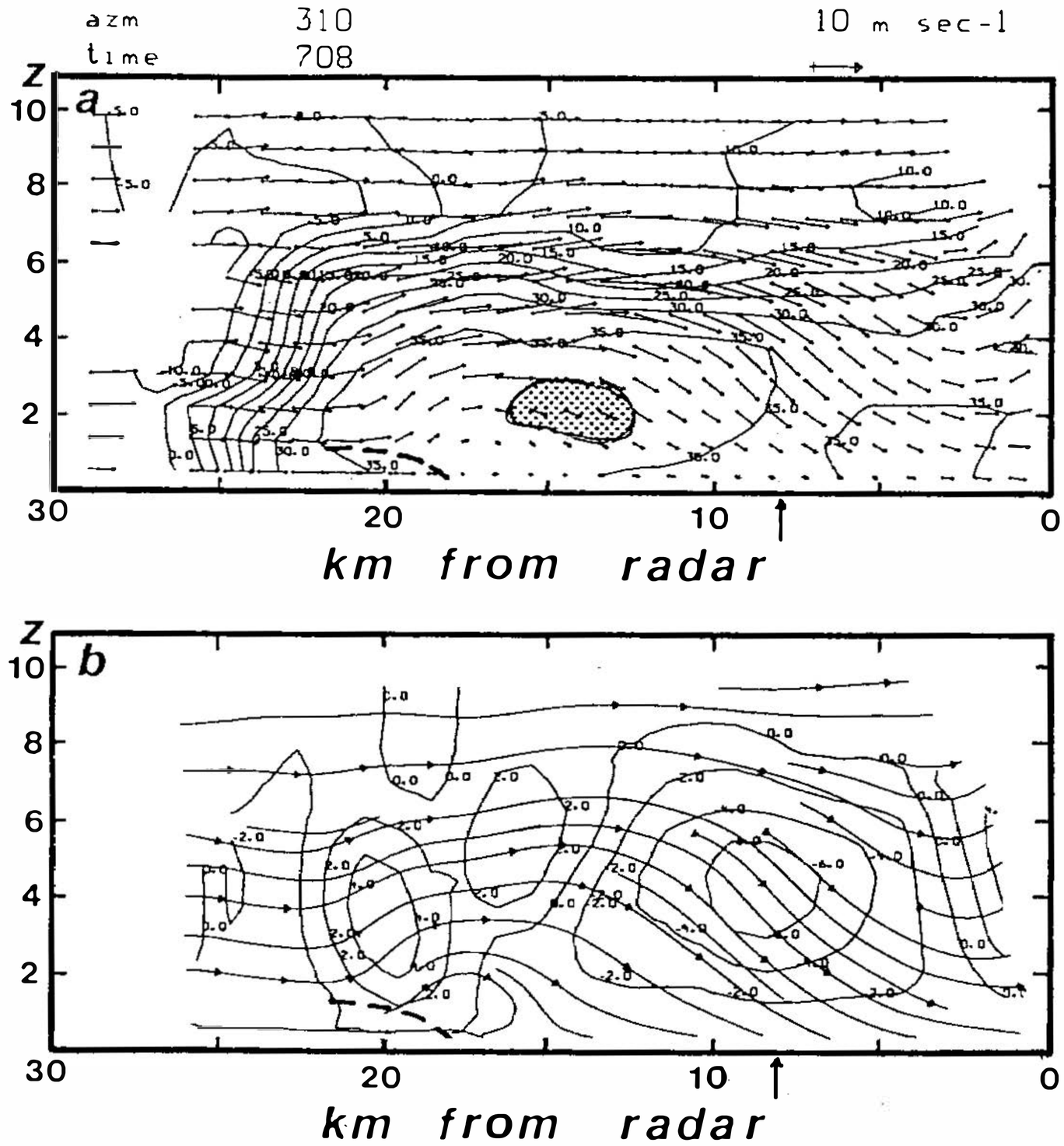

Fig. 7. As in Figure 4 except for the single-Doppler analysis at 0708 LST 25 June.

the high reflectivity region is confined to the area below 6 km and ahead of the front. The strength of convective cells decreases slightly, but there is still a broad region of reflectivities above 35 dBZ ahead of the Mei-Yu front. The rear-to-front flow described in the last figure weakens as the updraft over the Mei-Yu front lowers.

The next two time periods (0716 LST and 0724 LST) are shown in Figures 8 and 9. The figures indicate that although the updraft weakens somewhat (> 2 m s^{-1}), it regains its strength and remains vertically oriented. The downdraft still coincides with the high reflectivity core over the gust front and retains its strength (4—6 m s^{-1}). As shown in the previous figures the dry air intrusion above 6 km continues to push towards the radar. At 0724 LST (Figure 9), the dry air intrusion is over the top of the Mei-Yu front. The low-level rear-to-front flow associated with the cold air continues to enhance the flow into the Mei-Yu front as described above. Additionally, a convective cell is located near the gust front at 6 km as shown by the region of high reflectivities (> 40 dBZ) in that region.

The Mei-Yu front has moved to 17 km at 0732 LST (Figure 10), 6 km ahead of the initial scan at 0653 LST (Figure 6). Also advancing along with the front was the region of maximum radial velocity. The strong wind maximum near 5 km ASL was centered near 14 km in the initial scan and is located near 7 km with a maximum of −18 m s^{-1} in this final figure. The updraft associated with the Mei-Yu front once again weakens slightly, as does the downdraft associated with the gust front, but each feature retains its character throughout the period. The dry air intrusion seen in the previous figures above 6 km has extended well over the Mei-Yu front, nearly reaching the gust front. Below it, the reflectivities remain above 35 dBZ between the Mei-Yu front and the gust front.

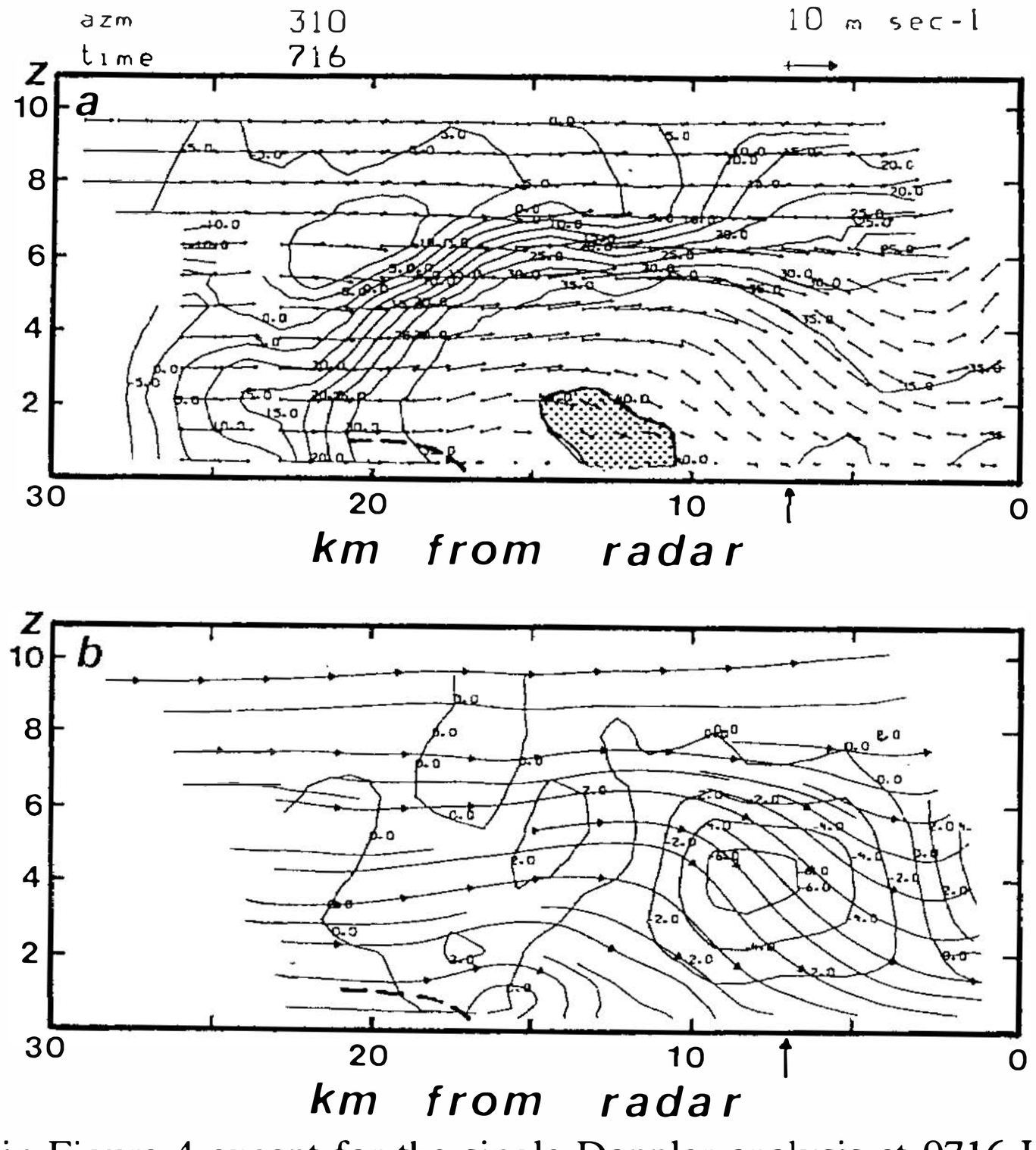

Fig. 8. As in Figure 4 except for the single-Doppler analysis at 0716 LST 25 June.

4. SUMMARY AND CONCLUSIONS

From previous six figures, two important features of the Mei-Yu front and the associated prefrontal rainband become apparent. The first is that strong northwesterly mid-level winds push the precipitation products ahead of the Mei-Yu front rather than behind it. Additionally this strong mid-level flow moves with the Mei-Yu front, remaining just ahead of the Mei-Yu front throughout the entire period. The second important feature is a dry layer above 6 km, as shown by the low reflectivities, overlaying the Mei-Yu front and the associated prefrontal rainband. This dry layer is enhanced as this layer dried out even further as a tongue of much drier air pushes over the Mei-Yu front. These two features combine to create the gust front ahead of the Mei-Yu front. The dry air above 6 km causes the air to evaporatively cool and descend. The precipitation loading in the high-reflectivity region ahead of the Mei-Yu front further increases the negative buoyancy of the descending air. The combined effects of evaporative cooling and precipitation loading maintain the convective downdrafts in a broad region ahead of the Mei-Yu front. The descending cool downdraft air results in a horizontally diverging cold outflow at the lowest level. Part of this diverging cold outflow moves toward the southeast, interacting with the moisture-rich southwest monsoon flow to create a gust front ahead of the Mei-Yu front. At the same time, the gust front also enhances the convergence at the Mei-Yu front by redirecting some of the strong rear-to-front flow aloft back toward the Mei-Yu front. This redirected flow enhances the convergence at the Mei-Yu front.

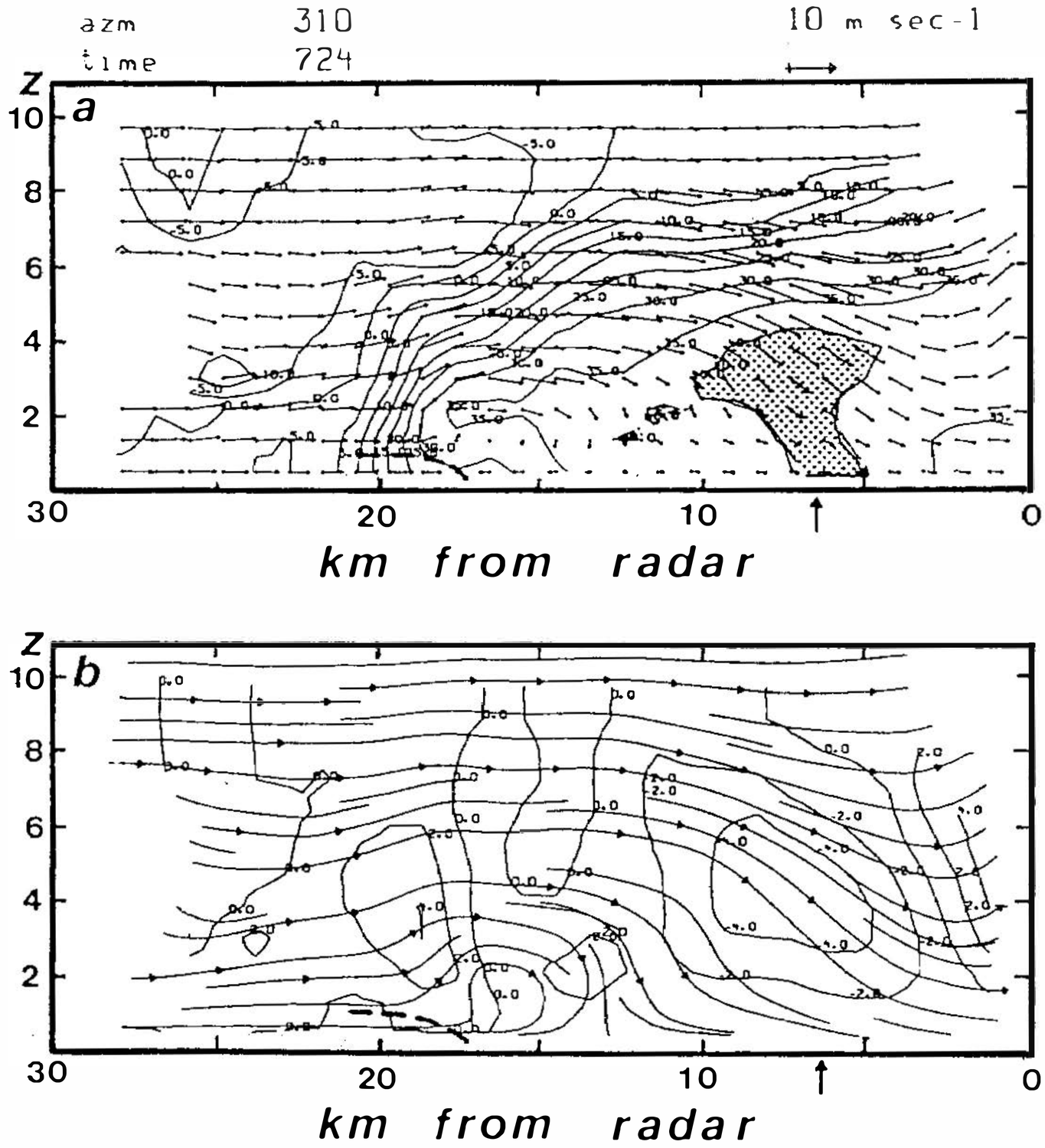

Fig. 9. As in Figure 4 except for the single-Doppler analysis at 0724 LST 25 June.

The results of a comparison of a single- and dual-Doppler analysis techniques show that a single-Doppler analysis can extract qualitative information about the kinematic structures of the convective rainband that occurred during TAMEX IOP 13. Comparison of RHI sections along the same radial shows that the main structural features of the storm as revealed by dual-Doppler radar data are also recovered by the single-Doppler analysis technique. Using the horizontal and vertical winds, reflectivity and streamline fields recovered from a single-Doppler analysis over a 40 min time span, the kinematic structure and time history of a prefrontal convective rainband during IOP 13 was examined. The results show that a combination of evaporative cooling and precipitation loading is mainly responsible for maintaining the convective downdrafts in a broad area ahead of the Mei-Yu front. The descending air of each convective downdraft carried much cooler air of the convective downdraft from middle and upper layers with it. As the descending air approached the surface, it spread out horizontally, forming a cold outflow in the boundary layer. Part of this cold outflow moved southeastward, interacting with the southwest monsoon flow to form a gust front. As discussed in Part I, new cells form at the GF and eventually merge with the old cells behind the GF, thereby prolonging the life span of the prefrontal rainband. The northwestward branch of the surface cold outflow enhanced the low-level convergence at the leading edge of the front (see Figure 8 in Lin *et al.* 1993). As a result, upward motion continually prevailed at the front. The frontal updraft was tilted toward the southeast with the environmental shear vector at heights greater than 3 km. This tilted updraft in turn resulted in a high reflectivity

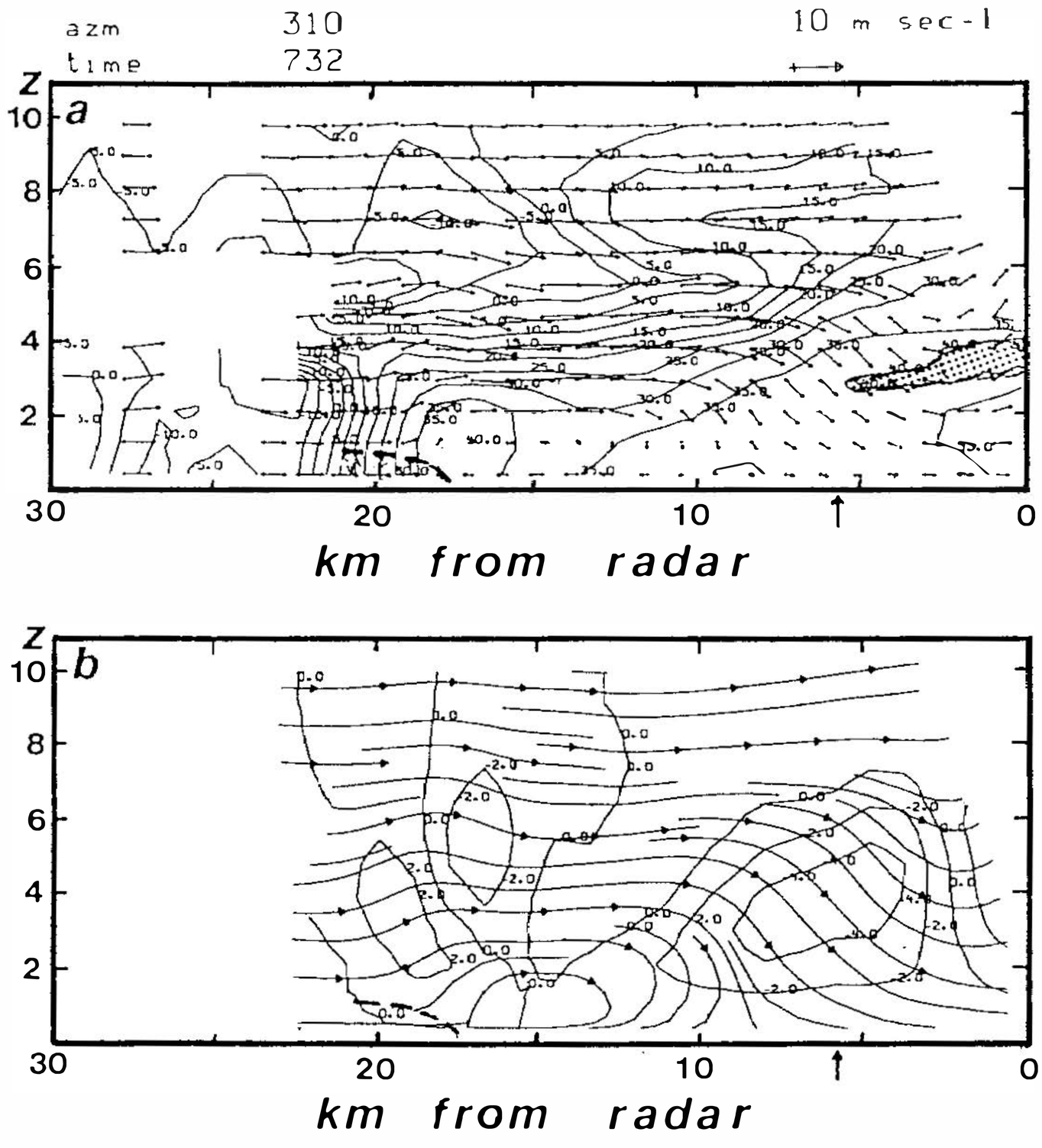

Fig. 10. As in Figure 4 except for the single-Doppler analysis at 0732 LST 25 June.

core ahead of the front creating a convective downdraft in a manner described above. The interplay between the convective updraft and downdraft in the manner described above was largely responsible for sustaining the life cycle of the rainband as it traveled down the central west coast.

The aforementioned phenomena involving the low-level horizontal cold outflows in promoting new convection at the GF and enhancing the convergence at the front were unique to this study. In this study we have focused on the structural features of the airflow, reflectivity distribution and the low-level convergence/divergence using single-Doppler measurements over a period of 46 minutes. Results show that the overall structural features of the rainband, as seen from the cross-section in a direction normal to the Mei-Yu front, are consistent with those presented in the dual-Doppler studies by Lin *et al.* (1992) and Lin *et al.* (1993) at 0653 and 0701 LST. In particular, we have confirmed that three relevant physical mechanisms, including the effects of 1) frontal lifting; 2) a GF arising from the convective downdraft ahead of the front; and 3) discrete developments in advance of the line, are mainly responsible for maintaining this long-lived rainband during the mature stage of its life cycle. These features are the essential components of the conceptual model proposed by Lin *et al.* (1992).

Acknowledgments The authors wish to express their appreciation to those scientists, technicians and staff members who participated in the TAMEX project. We would like to thank the National Center for Atmospheric Research (NCAR) for providing Doppler data

and technical assistance. Special thanks go to the National Science Council of the Republic of China and the National Science Foundation for supporting the field experiment. We are grateful to Hsi Shen, Hsiu-Wu Chang, Mike Miglioranzi, Joe Zilka, Mike Beeson, and Marty Martino of Saint Louis University for their help in data processing. This work was supported by the Atmospheric Science Division, National Science Foundation, under NSF Grant ATM-9012135, and a National Aeronautical and Space Administrations JOVE (Joint Venture) project grant.

REFERENCES

Browning, K. A., and T. W. Harrold, 1970: Air motion and precipitation growth at a cold front. *Q. J. Roy. Meteor. Soc.*, **96**, 369-389.

Li, J., Y.-L. Chen, and W. C. Lee, 1995: Analysis of a heavy rainfall event during TAMEX. Proc. Int'l Workshop on Heavy Rainfall in East Asia, 27-29 March 1995, Seoul, Korea, 82-89.

Lin, Y. J., T. C. Wang, and J. H. Lin, 1986: Pressure and temperature perturbations within a squall line thunderstorms derived from SESAME dual-Doppler data. *J. Atmos. Sci.*, **43**, 2302-2327.

Lin, Y. J., R. W. Pasken, and H. W. Chang, 1992: The structure of a subtropical prefrontal convective rainband. Part I: Mesoscale kinematic structure determined from dual-Doppler measurements. *Mon. Wea. Rev.*, **120**, 1816-1836.

Lin, Y. J., H. W. Chang, and R. W. Pasken, 1993: The structure of a subtropical prefrontal convective rainband. Part II: Dynamic and thermodynamic structures and momentum budgets. *Mon. Wea. Rev.*, **121**, 1671-1687.

Lin, Y. J., R. W. Pasken, J. G. Zilka, and M. R. Martino, 1996: Further studies of a pre-frontal convective rainband during TAMEX IOP 13. Part I: Reflectivity history and cell evolution. *TAO*, **7**, 61-82.

Maddox, R. A., 1980: Mesoscale convective complexes. *Bull. Am. Meteor. Soc.*, **61**, 1374-1387.

Ray, P. S., C. L. Ziegler, W. Bumgarner, and R. J. Serafin, 1980: Single and multiple Doppler radar observations of tornadic storms. *Mon. Wea. Rev.*, **108**, 1607-1625.

Wakimoto, R. M., 1982: The life cycle of a thunderstorm gust front as viewed with Doppler radar and rawindsonde data. *Mon. Wea. Rev.*, **110**, 1060-1082.

Ziegler, C. L., P. S. Ray, and N. C. Knight, 1983: Hail growth in an Oklahoma multicell storm. *J. Atmos. Sci.*, **40**, 1768-1791.